# Efficient Bayesian-based multiview deconvolution

Stephan Preibisch[1–4], Fernando Amat[2], Evangelia Stamataki[1], Mihail Sarov[1], Robert H Singer[2–4], Eugene Myers[1,2] & Pavel Tomancak[1]

**Light-sheet fluorescence microscopy is able to image large specimens with high resolution by capturing the samples from multiple angles. Multiview deconvolution can substantially improve the resolution and contrast of the images, but its application has been limited owing to the large size of the data sets. Here we present a Bayesian-based derivation of multiview deconvolution that drastically improves the convergence time, and we provide a fast implementation using graphics hardware.**



Modern light-sheet microscopes[1–3] acquire images of large, developing specimens with high temporal and spatial resolution typically by imaging them from multiple directions (**Fig. 1a**). Deconvolution uses knowledge about the optical system to increase spatial resolution and contrast after acquisition. An advantage unique to light-sheet microscopy, particularly the selective-plane illumination microscopy (SPIM) variant, is the ability to observe the same location in the specimen from multiple angles, which renders the ill-posed problem of deconvolution more tractable[4–10].

Richardson-Lucy (RL) deconvolution[11,12] (**Supplementary Note 1**) is a Bayesian-based derivation resulting in an iterative expectation-maximization (EM) algorithm[5,13] that is often chosen for its simplicity and performance. Multiview deconvolution has previously been derived using the EM framework[5,9,10]; however, the convergence time of the algorithm remains orders of magnitude longer than the time required to record the data. We addressed this problem by deriving an optimized formulation of Bayesian-based deconvolution for multiple-view geometry that explicitly incorporates conditional probabilities between the views (**Fig. 1b**,**c** and **Supplementary Fig. 1**) and combining it with ordered subsets EM (OSEM)[6] (**Fig. 1d** and **Supplementary Fig. 2**), achieving substantially faster convergence (**Fig. 1d**–**f**).

Bayesian-based deconvolution models images and point spread functions (PSFs) as probability distributions. The goal is to estimate the most probable underlying distribution (deconvolved image) that best explains all observed distributions (views) given their conditional probabilities (PSFs). We first rederived the original RL deconvolution algorithm and subsequently extended it to multiple-view geometry, yielding

$$f_{\mathrm{RL}}^{v}(\xi) = \int_{x_v} \frac{\phi_v(x_v)}{\int_{\xi} \psi^{r}(\xi) P(x_v \mid \xi) \mathrm{d}\xi} P(x_v \mid \xi) \mathrm{d}x_v \quad (1)$$

$$\psi^{r+1}(\xi) = \psi^{r}(\xi) \prod_{v \in V} f_{\mathrm{RL}}^{v}(\xi) \quad (2)$$

where $\psi^{r}(\xi)$ denotes the deconvolved image at iteration $r$ and $\phi_v(x_v)$ denotes the input views, both as functions of their respective pixel locations $\xi$ and $x_v$, whereas $P(x_v|\xi)$ denotes the individual PSFs (**Supplementary Note 1**). Equation (1) denotes a classical RL update step for one view; equation (2) illustrates the combination of all views into one update of the deconvolved image (**Supplementary Video 1**). In contrast to the maximum-likelihood (ML) EM[5,13] that combines RL updates by addition, equation (2) suggests a multiplicative combination. We proved that equation (2), just as the ML-EM[5,13] algorithm, converges to the ML solution (**Supplementary Note 2**). The ML solution is not necessarily the correct solution if disturbances such as noise or misalignments are present in the input images (**Fig. 2**). Importantly, previous extensions to multiple views[5–10] assume individual views to be independent observations (**Supplementary Fig. 2**). Assuming independence between two views implies that by observing one view, nothing can be learned about the other view. We showed that this independence assumption is not required to derive equation (2) (**Supplementary Note 3**). Our solution represents, to our knowledge, the first complete derivation of RL multiview deconvolution based on probability theory and Bayes' theorem.

As we do not need to consider views to be independent, we next asked whether the conditional probabilities describing the relationship between two views can be modeled and used to improve convergence behavior (**Supplementary Figs. 1** and **3** and **Supplementary Notes 3** and **4**). If we assume that a single photon is observed in the first view, the PSF of this view and Bayes' theorem can be used to assign a probability to every location in the deconvolved image having emitted this photon (**Fig. 1b**). On the basis of this probability distribution, the PSF of the second view directly yields the probability distribution describing where to expect a corresponding observation for the same fluorophore in the second view (**Fig. 1b**). Thus, we argue that it is possible to compute an approximate image ('virtual' view) of one view from another view provided that the PSFs of both views are known (**Fig. 1c**).

We used these virtual views to perform intermediate update steps at no additional computational cost, decreasing

[1]Max Planck Institute of Molecular Cell Biology and Genetics, Dresden, Germany. [2]Janelia Farm Research Campus, Howard Hughes Medical Institute, Ashburn, Virginia, USA. [3]Department of Anatomy and Structural Biology, Albert Einstein College of Medicine, Bronx, New York, USA. [4]Gruss Lipper Biophotonics Center, Albert Einstein College of Medicine, Bronx, New York, USA. Correspondence should be addressed to S.P. (preibischs@janelia.hhmi.org) or P.T. (tomancak@mpi-cbg.de).

RECEIVED 8 JULY 2013; ACCEPTED 6 MARCH 2014; PUBLISHED ONLINE 20 APRIL 2014; DOI:10.1038/NMETH.2929

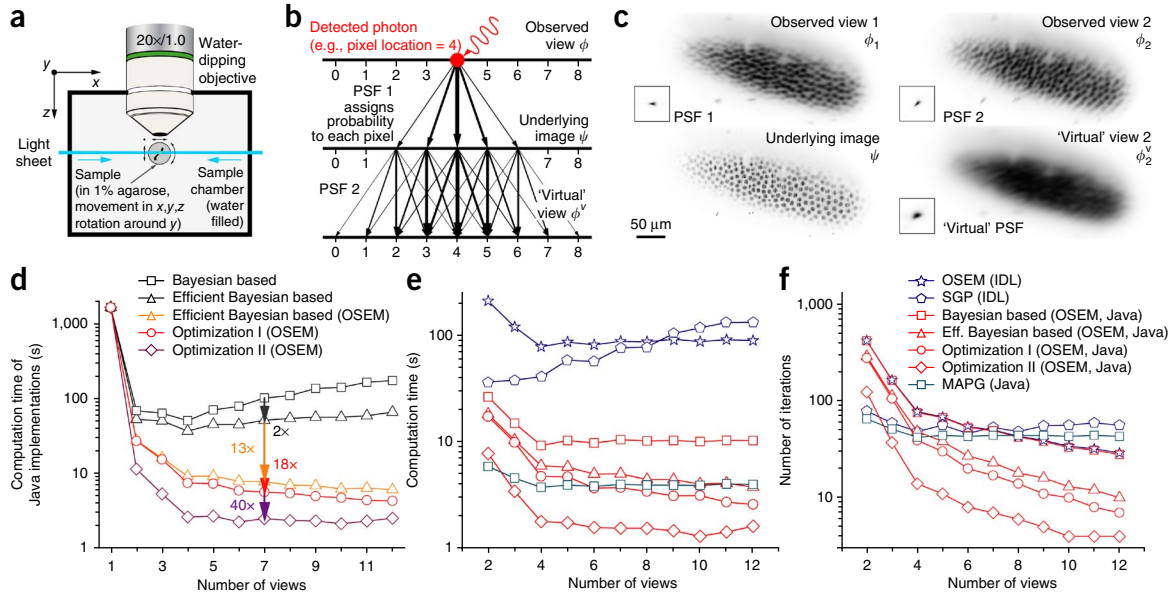


**Figure 1** | Principles and performance. (**a**) Basic layout of a light-sheet microscope capable of multiview acquisitions. (**b**) Illustration of 'virtual' views. A photon detected at a certain location in a view was emitted by a fluorophore in the sample; the PSF assigns a probability to every location in the underlying image having emitted that photon. Consecutively, the PSF of any other view assigns to each of its own locations the probability to detect a photon corresponding to the same fluorophore. (**c**) Example of an entire virtual view computed from observed view 1 and the knowledge of PSF 1 and PSF 2. (**d**) Convergence time of the different Bayesian-based methods. We used a known ground-truth image (**Supplementary Fig. 5**) and let all variations converge until they reached precisely the same quality. The increase in computation time for an increasing number of views of the combined methods (black) is due to the fact that with an increasing number of views, more computational effort is required to perform one update of the deconvolved image (**Supplementary Fig. 4**) (**e**) Convergence times for the same ground-truth image of our Bayesian-based methods compared to those of other optimized multiview deconvolution algorithms[5–8]. The difference in computation time between Java implementations and IDL implementations, OSEM[6] and SGP[8], results in part from nonoptimized IDL code. (**f**) Corresponding number of iterations for our algorithm and other optimized multiview deconvolution algorithms.

the computational effort approximately twofold (**Fig. 1d** and **Supplementary Note 4**). The multiplicative combination (equation (2)) directly suggests a sequential approach, wherein each RL update (equation (1)) is directly applied to $\psi^r(\xi)$ (**Supplementary Fig. 2** and **Supplementary Note 5**). This sequential scheme is equivalent to the OSEM[6] algorithm and results in a 13-fold decrease in convergence time. This gain increases linearly with the number of views[6] (**Fig. 1d** and **Supplementary Fig. 4**). To further reduce convergence time, we introduced *ad hoc* simplifications (optimizations I and II) for the estimation of conditional probabilities that achieve up to 40-fold improvement compared to deconvolution methods that assume view independence (**Fig. 1d–f**, **Supplementary Figs. 4** and **5** and **Supplementary Notes 6** and **7**). The new algorithm also performs well in the presence of noise and imperfect PSFs (**Supplementary Figs. 6–8**). If the input views show a very low signal-to-noise ratio (SNR), atypical for SPIM, the speedup is preserved, but the quality of the deconvolved image is reduced. Our Bayesian-based derivation does not assume a specific noise model, but it is in practice robust with respect to Poisson noise, which is the dominating source of noise in light-sheet microscopy acquisitions.

We compared the performance of our method with that of previously published multiview deconvolution algorithms[5–10] in terms of convergence behavior and run time on the central processing unit (CPU) (**Figs. 1e**,**f** and **2d** and **Supplementary Figs. 4b** and **9a**,**b**). For typical SPIM multiview scenarios consisting of around seven views with a high SNR, our method requires sevenfold fewer iterations and is at least threefold faster than OSEM[6], scaled gradient projection (SGP)[8] and maximum a posteriori with Gaussian noise (MAPG)[7]. At the same time our optimization is able to improve the image quality of real and simulated data sets compared to MAPG[7] (**Fig. 2e**,**f** and **Supplementary Fig. 9c–h**). A further speedup of threefold and reduced memory consumption is achieved by using our CUDA (Compute Unified Device Architecture) implementation (**Supplementary Fig. 10g**). Moreover, our approach is capable of dealing with partially overlapping acquisitions typical in multiview imaging (**Supplementary Fig. 10** and Online Methods).

In order to evaluate our algorithm on realistic three-dimensional (3D) multiview image data, we simulated a ground-truth data set resembling a biological specimen (**Fig. 2a**). We next simulated image acquisition in a SPIM microscope from multiple angles by applying signal attenuation across the field of view, convolving the data with the PSF of the microscope, simulating the multiview optical sectioning and using a Poisson process to generate the final pixel intensities (**Fig. 2b** and Online Methods). We deconvolved the generated multiview data (**Fig. 2c**) using our algorithm with and without regularization (regularization adds smoothness constraints to the deconvolution process to achieve a more plausible solution for this ill-posed problem) and compared the results to the content-based fusion[14] and the MAPG[7] deconvolution (**Fig. 2d–f**). Our algorithm reached optimal reconstruction quality faster (**Fig. 2d**) and introduced fewer artifacts than MAPG[7] (**Fig. 2e**,**f** and **Supplementary Videos 2** and **3**). Tikhonov regularization[15] was required to converge to a reasonable result under realistic imaging conditions (**Fig. 2d–f**).

We applied our deconvolution approach to multiview SPIM acquisitions of *Drosophila melanogaster* and *Caenorhabditis*

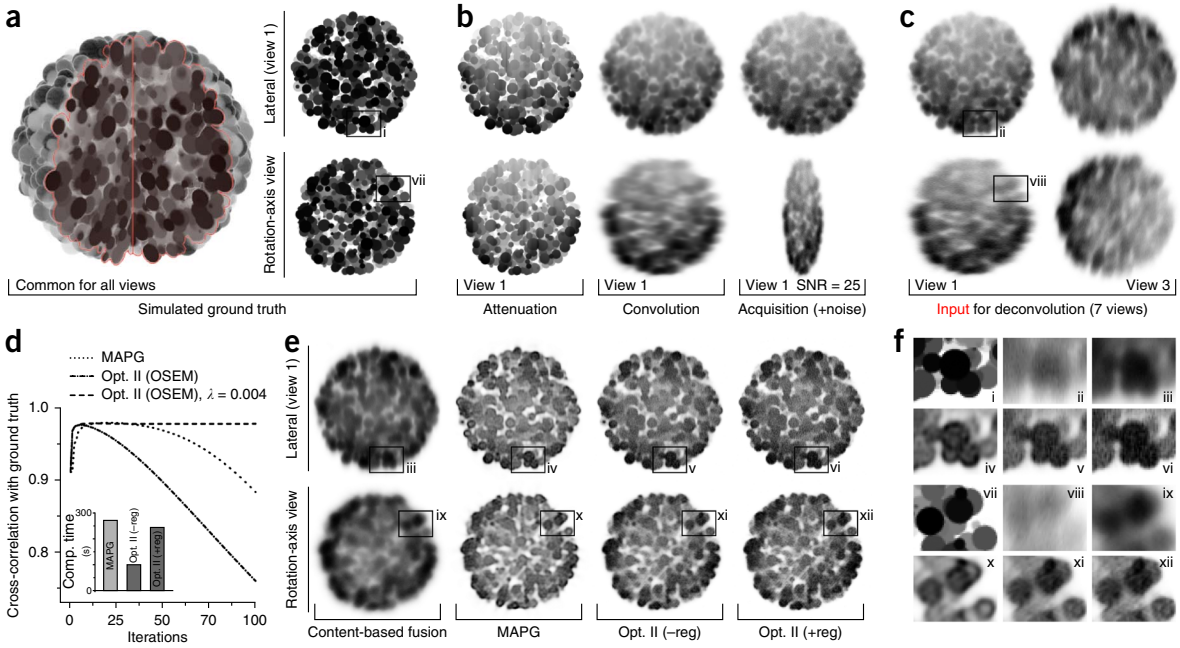


**Figure 2** | Deconvolution of simulated 3D multiview data. (**a**) Left, 3D rendering of a computer-generated volume resembling a biological specimen. The red outlines mark the wedge removed from the volume to show the content inside. Right, sections through the generated volume in the lateral direction (as seen by the SPIM camera, top) and along the rotation axis (bottom). (**b**) Same slices as in **a** with illumination attenuation applied (left), convolved with a PSF of a SPIM microscope (center) and simulated using a Poisson process (right). The bottom right panel shows the unscaled simulated light-sheet sectioning data along the rotation axis. (**c**) Slices from views 1 and 3 of the seven views generated from **a** by applying processes pictured in **b** and rescaling to isotropic resolution. These seven volumes are the input to the fusion and deconvolution algorithms quantified in **d** and visualized in **e**. (**d**) Cross-correlation of deconvolved and ground-truth data as a function of the number of iterations for MAPG[7] and our algorithm with and without regularization (reg). The inset compares the computation (comp.) time. (Both algorithms were implemented in Java to support partially overlapping data sets; **Supplementary Fig. 10**). (**e**) Slices equivalent to **c** after content-based fusion[14] (first column), MAPG[7] deconvolution (second column), our approach without regularization (third column) and with regularization[15] (fourth column; Tikhonov[15] regularization parameter λ = 0.004). (**f**) Areas marked by boxes in **a**,**c**,**e** at higher magnification. Note the increased artificial ring patterns in MAPG[7].

*elegans* embryos (**Fig. 3a–e**). We achieved a substantial increase in contrast as well as resolution with respect to the content-based fusion[14] (**Fig. 3b** and **Supplementary Fig. 11**); only a few iterations were required and computation times were typically in the range of a few minutes per multiview acquisition (**Supplementary Table 1**). We applied the deconvolution to a four-view acquisition of a fixed *C. elegans* in larval stage 1 (L1) expressing GFP-tagged lamin (LMN-1–GFP) labeling the nuclear lamina and stained for DNA with Hoechst (**Fig. 3f,g**). Multiview deconvolution improved contrast and resolution compared to the input data and enabled unambiguous segmentation of nuclei in problematic areas of the nervous system[16] (**Supplementary Videos 4–7**). The algorithm dramatically improved multiview data acquired with OpenSPIM[17] (**Supplementary Fig. 12**), and its efficiency makes it applicable to spatially large multiview data sets (**Supplementary Fig. 13**) and to processing of long-term time lapses from the Zeiss Lightsheet Z.1 (**Supplementary Videos 8–11** and **Supplementary Table 1**).

Multiview deconvolution increases contrast in SPIM data after acquisition, complementary to hardware-based contrast enhancement achieved by digital scanned laser light-sheet microscopy (DSLM-SI)[18] (**Supplementary Fig. 14**). Moreover, multiview deconvolution produced superior results when comparing an acquisition of the same sample with SPIM and a two-photon microscope (**Supplementary Fig. 15**). Finally, the benefits of the multiview deconvolution approach are not limited to SPIM, as illustrated by the deconvolved multiview spinning disc confocal microscope acquisition of a *C. elegans* in L1 stage[14] (**Supplementary Fig. 16**).

A major obstacle for widespread application of deconvolution approaches to multiview light-sheet microscopy data is the lack of usable and scalable multiview deconvolution software. Therefore, we implemented our fast converging algorithm as a Fiji[19] plug-in taking advantage of ImgLib2 (ref. 20) and GPU processing (http://fiji.sc/Multi-View_Deconvolution). The only free parameter of the method that must be chosen by the user is the number of iterations for the deconvolution process. We facilitate this choice by providing a debug mode allowing the user to inspect all intermediate iterations and identify optimal trade-off between quality and computation time. Our Fiji[19] implementation synergizes with other related plug-ins and provides an integrated solution for the processing of multiview light-sheet microscopy data of arbitrary size.

## METHODS

Methods and any associated references are available in the online version of the paper.

*Note: Any Supplementary Information and Source Data files are available in the online version of the paper.*


### ACKNOWLEDGMENTS

We thank T. Pietzsch (Max Planck Institute of Molecular Cell Biology and Genetics (MPI-CBG)) for helpful discussions, proofreading and access to his unpublished software; N. Clack, F. Carrillo Oesterreich and H. Bowne-Anderson for discussions; N. Maghelli for two-photon imaging; P. Verveer (MPI Dortmund) for source

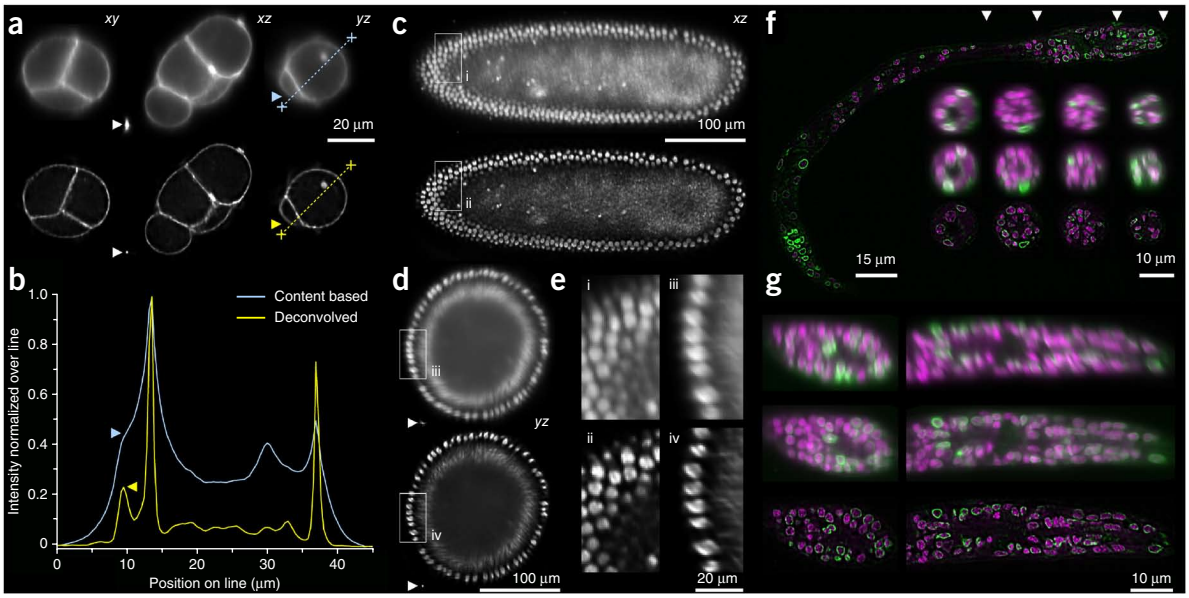


**Figure 3** | Application to biological data. (**a**) Comparison of reconstruction results using content-based fusion[14] (top row) and multiview deconvolution (bottom row) on a four-cell–stage *C. elegans* embryo expressing a PH domain–GFP fusion marking the membranes. Dotted lines mark plots shown in **b**; white arrowheads mark PSFs of a fluorescent bead before and after deconvolution. (**b**) Line plot through the volume along the rotation axis (*yz*, contrast locally normalized). This orientation typically shows the lowest resolution of a fused data set in light-sheet acquisitions, as all input views are oriented axially (**Supplementary Fig. 11**). SNR is substantially enhanced; arrowheads mark points illustrating increased resolution. (**c**,**d**) Cut planes through a blastoderm-stage *Drosophila* embryo expressing His-YFP in all cells. (**e**) Magnified view on parts of the *Drosophila* embryo. The left panel is a view in lateral orientation of one of the input views; the right panel shows a view along the rotation axis characterized by the lowest resolution. (**f**,**g**) Comparison of deconvolution and input data of a fixed L1 *C. elegans* larva expressing LMN-1–GFP (green) and stained with Hoechst (magenta). (**f**) Single slice through the deconvolved data set; arrowheads mark four locations of transversal cuts shown below. The cuts compare two orthogonal input views (0°, 90°) with the deconvolved data. No input view offers high resolution in this orientation approximately along the rotation axis. (**g**) The left box in the first row shows a random slice of a view in axial orientation (worst resolution). The second row shows a view in lateral orientation (best resolution). The third row shows the corresponding deconvolved image. The right boxes each show a slice through the nervous system. The alignment of the *C. elegans* L1 data set was refined using nuclear positions (Online Methods). The *C. elegans embryo* (**a**,**b**) and the *Drosophila* embryo (**d**,**e**) are each one time point of a time series (none of the other time points is used in this paper). The *C. elegans* L1 larva (**f**,**g**) is an individual acquisition of one fixed sample.

code and helpful discussions; M. Weber for imaging the *Drosophila* time series; S. Jaensch for preparing the *C. elegans* embryo; J.K. Liu (Cornell University) for the LW698 strain; S. Saalfeld for help with 3D rendering; P.J. Keller for supporting F.A. and for the DSLM-SI data set; A. Cardona for access to his computer; and Carl Zeiss Microimaging for providing us with the SPIM prototype. S.P. was supported by MPI-CBG in P.T.'s lab, Howard Hughes Medical Institute (HHMI) in E.M.'s lab and the Human Frontier Science Program (HFSP) Postdoctoral Fellowship LT000783/2012 in R.H.S.'s lab, with additional support from US National Institutes of Health (NIH) GM57071. F.A. was supported by HHMI in P.J. Keller's lab. E.S. and M.S. were supported by MPI-CBG. R.H.S. was supported by NIH grants GM057071, EB013571 and NS083085. E.M. was supported by HHMI and MPI-CBG. P.T. was supported by The European Research Council Community's Seventh Framework Program (FP7/2007-2013) grant agreement 260746 and the HFSP Young Investigator grant RGY0093/2012. M.S., E.M. and P.T. were additionally supported by the Bundesministerium für Bildung und Forschung grant 031A099.

## AUTHOR CONTRIBUTIONS

S.P. and F.A. derived the equations for multiview deconvolution. S.P. implemented the software and performed all analysis, and F.A. implemented the GPU code. E.S. generated and imaged the H2Av-mRFPruby fly line. M.S. prepared, and M.S. and S.P. imaged, the *C. elegans* L1 sample. S.P. and P.T. conceived the idea and wrote the manuscript. R.H.S. provided support and encouragement, E.M. and P.T. supervised the project.

## COMPETING FINANCIAL INTERESTS

The authors declare no competing financial interests.



1. Huisken, J., Swoger, J., Del Bene, F., Wittbrodt, J. & Stelzer, E.H.K. *Science* **305**, 1007–1009 (2004).
2. Keller, P.J., Schmidt, A.D., Wittbrodt, J. & Stelzer, E.H.K. *Science* **322**, 1065–1069 (2008).
3. Truong, T.V., Supatto, W., Koos, D.S., Choi, J.M. & Fraser, S.E. *Nat. Methods* **8**, 757–760 (2011).
4. Swoger, J., Verveer, P., Greger, K., Huisken, J. & Stelzer, E.H.K. *Opt. Express* **15**, 8029–8042 (2007).
5. Shepp, L.A. & Vardi, Y. *IEEE Trans. Med. Imaging* **1**, 113–122 (1982).
6. Hudson, H.M. & Larkin, R.S. *IEEE Trans. Med. Imaging* **13**, 601–609 (1994).
7. Verveer, P.J. *et al. Nat. Methods* **4**, 311–313 (2007).
8. Bonettini, S., Zanella, R. & Zanni, L. *Inverse Probl.* **25**, 015002 (2009).
9. Krzic, U. *Multiple-View Microscopy with Light-Sheet Based Fluorescent Microscope*. PhD thesis, Univ. Heidelberg (2009).
10. Temerinac-Ott, M. *et al. IEEE Trans. Image Process.* **21**, 1863–1873 (2012).
11. Richardson, W.H. *J. Opt. Soc. Am.* **62**, 55–59 (1972).
12. Lucy, L.B. *Astron. J.* **79**, 745–754 (1974).
13. Dempster, A.P., Laird, N.M. & Rubin, D.B. *J. R. Stat. Soc. Series B Stat. Methodol.* **39**, 1–38 (1977).
14. Preibisch, S., Saalfeld, S., Schindelin, J. & Tomancak, P. *Nat. Methods* **7**, 418–419 (2010).
15. Tikhonov, A.N. & Arsenin, V.Y. *Solutions of Ill-Posed Problems* (Winston, 1977).
16. Long, F., Peng, H., Liu, X., Kim, S. & Myers, E. *Nat. Methods* **6**, 667–672 (2009).
17. Pitrone, P.G. *et al. Nat. Methods* **10**, 598–599 (2013).
18. Keller, P.J. *et al. Nat. Methods* **7**, 637–642 (2010).
19. Schindelin, J. *et al. Nat. Methods* **9**, 676–682 (2012).
20. Pietzsch, T., Preibisch, S., Tomancak, P. & Saalfeld, S. *Bioinformatics* **28**, 3009–3011 (2012).

## ONLINE METHODS

**Derivations and proof.** The efficient Bayesian-based multiview deconvolution is an extension of the classical Richardson-Lucy[11,12] deconvolution, which is based on probability theory and Bayes' theorem. We rederive the single-view Bayesian-based deconvolution and extend it to multiple views (**Supplementary Note 1**), and prove the convergence of our new derivation to the maximum-likelihood solution (**Supplementary Note 2**). We show that the Bayesian-based multiview deconvolution can be derived without assuming independence of the input views (**Supplementary Note 3**) and that the conditional probabilities can subsequently be incorporated into the derivation using 'virtual' views (**Fig. 1c**, **Supplementary Figs. 1** and **2** and **Supplementary Note 4**). Finally, we discuss further optimizations (**Supplementary Notes 5** and **6**) and perform extensive benchmarks and comparisons (**Supplementary Figs. 4–9** and **17** and **Supplementary Note 7**).

**Multiview registration and PSF estimation.** Prerequisite for multiview deconvolution of light-sheet microscopy data are precisely aligned multiview data sets and estimates of point spread functions (PSFs) for all views. We exploit the fact that for the purposes of registration we include subresolution fluorescent beads into the rigid agarose medium in which the specimen is embedded. The beads are initially used for multiview registration of the SPIM data[14] and subsequently to extract the PSF for each view for the purposes of multiview deconvolution. We average the intensity of PSFs for each view for all the beads that were identified as corresponding during registration, yielding a precise measure of the PSF for each view under the specific experimental condition. This synergy of registration and deconvolution ensures realistic representation of PSFs under any imaging condition. Alternatively, simulated PSFs or PSFs measured by other means can be provided as inputs to the deconvolution algorithm.

**Multiview deconvolution and other optical sectioning microscopy.** In order to better characterize the gain in resolution and contrast of multiview deconvolution, several experiments and comparisons were performed. We compared a SPIM multiview acquisition to a single-view two-photon microscopy acquisition of the same sample (**Supplementary Fig. 15**). The fixed *Drosophila* embryo stained with Sytox green was embedded in agarose and first imaged using a 20×/0.5-NA (numerical aperture) water-dipping objective in the Zeiss SPIM prototype. After acquisition the agarose was cut, and the same sample was imaged using a two-photon microscope and a 20×/0.8-NA air objective. The data sets were aligned using the fluorescent beads visible in both the SPIM and two-photon acquisitions. The SPIM data set was reconstructed using content-based fusion[14] and multiview deconvolution and was compared to the two-photon stack as well as the Richardson-Lucy single-view deconvolution[11,12] of the two-photon acquisition (**Supplementary Fig. 15**). Although two-photon microscopy is able to detect more photons in the center of the embryo, the multiview deconvolution shows substantially better resolution and coverage of the sample.

Multiview deconvolution can principally be applied to any optical sectioning microscope that is capable of sample rotation (**Supplementary Fig. 16**). We acquired a multiview data set using spinning disc confocal microscopy and a self-built rotational device[14]. We compared the quality of one individual input stack with the multiview deconvolution and the RL single-view deconvolution[11,12] of this stack. Although one view completely covers the sample, it is obvious that the multiview deconvolution clearly improves the resolution compared to the single-view deconvolution (**Supplementary Fig. 16d**).

**Gain in resolution due to multiview deconvolution.** To be able to quantify the gain in resolution, we analyzed images of fluorescent beads embedded in agarose (**Supplementary Fig. 11**). We extracted all corresponding fluorescent beads from seven input views, after multiview fusion[14] and after multiview deconvolution. Comparing the input views and the multiview fusion, it becomes apparent that the multiview fusion[14] reduces resolution in all dimensions except compared to the axial resolution of a single input view. On the other hand, the multiview deconvolution increases resolution in all dimensions compared to the multiview fused data. The multiview deconvolution achieves almost isotropic resolution in all dimensions comparable to the resolution of each input stack in the lateral direction.

**Partially overlapping multiview data sets.** In practical multiview deconvolution scenarios, where large samples are acquired, individual views often cover only some parts of the sample (**Fig. 3c–e** and **Supplementary Figs. 9** and **12–15**). The sequential update strategy (OSEM[6]) intrinsically supports partially overlapping data sets as it allows updating only parts of the deconvolved image using subsets of the input data. It is, however, necessary to achieve a balanced update for all pixels of the deconvolved image (**Supplementary Fig. 10a–f**).

Therefore, a weight image $w_v(\xi)$ is computed for each input view. It consists of a blending function returning 1 in central parts of a view; close to the boundaries, weights are decreasing from 1 to 0 following a cosine function and thus avoiding artifacts at image borders. By default, the sum of all weights for each pixel over all views is normalized, $\Sigma_{v \in V} w_v(\xi) = 1$, providing a balanced update of all pixels (**Supplementary Fig. 10a**,**b**). For each sequential update $v \in V$ contributed by one view $v$, the weight at every pixel location defines the fraction of the Richardson-Lucy[11,12] update that is applied to the deconvolved image

$$\psi^{r+1}(\xi) = \psi^{r}(\xi) w_v(\xi) f^{v}_{\mathrm{RL}}(\xi) \tag{3}$$

Normalizing the sum of weights to 1 is, however, equivalent to not using OSEM[6] in terms of performance (**Supplementary Fig. 10f**). In order to benefit from the OSEM[6] speedup, the weights have to be summed to values greater than 1. At the same time, individual weights for each view must be smaller or equal to 1 as the Bayesian-based iterative deconvolution becomes unstable otherwise. The OSEM[6] speedup that can be achieved is therefore dependent on the coverage of the deconvolved image by input views (**Supplementary Fig. 10b–f**). Choosing this number too high will lead to an uneven deconvolution, i.e., some parts of the sample will be more deconvolved than others (**Supplementary Fig. 10b–d**). In most cases the minimal number of overlapping views (**Supplementary Fig. 10c**) will provide a reasonable trade-off between speedup and uniformity. Some areas close to the boundaries

of the output image might still be less deconvolved in case they map to areas in the input views that are subject to the cosine blending function. However, those areas close to the boundaries in the input views typically contain only background.

In order to facilitate the choice of a reasonable number of overlapping data sets for a given acquisition, the Fiji[19] plug-in offers the option to output an image containing the number of contributing views at every pixel in the deconvolved image (**Supplementary Fig. 10e**). This also gives hints on how to adjust the imaging strategy regarding the number of views, size of stacks and their overlap. Please note that for smaller or more transparent specimens, data sets are usually completely overlapping (**Fig. 3a**,**b**,**f**,**g** and **Supplementary Fig. 16**).

**Simulation of SPIM data sets.** We simulate a 3D ground-truth data set that resembles a biological object such as an embryo or a spheroid (**Fig. 2a**). The simulated multiview microscope rotates the sample around the *x* axis, attenuates the signal, convolves the input, samples at lower axial resolution and creates the final sampled intensities using a Poisson process (**Fig. 2b**). Finally, the acquired 3D image is rotated back into the orientation of the ground-truth image, which corresponds to the task of multiview registration in real multiview data sets and results in the final input stacks for the multiview deconvolution (**Fig. 2c**). Computation time is measured until the maximal cross-correlation to the ground truth is achieved. Note that manual stopping of the deconvolution at earlier stages can reduce noise in the deconvolved image and optimize computation time.

To simulate the biological object, we use ImgLib2 (ref. 20) to draw a 3D sphere consisting of many small 3D spheres that have random locations, size and intensity. We simulate at twice the resolution of the final ground-truth image and downsample the result to avoid artificial edges.

An initial rotation around the *x* axis orients the ground truth-image so that the virtual microscope can perform an acquisition. However, every transformation of an image introduces artifacts owing to interpolation. Although on a real microscope this initial transformation is performed physically and thus does not introduce imaging artifacts, it is required for the simulation. To avoid the situation where artifacts are present in only the simulated views and not the ground-truth image (**Fig. 2a**), the ground-truth image is also rotated by 15° around the rotation axis of the simulated multiview microscope, i.e., all simulated input views are rotated by $(n + 15)°$ around the *x* axis.

The signal degradation along the light sheet is simulated using a simple physical model of light attenuation[21]. With an initial amount of laser power (or number of photons), the sample will absorb a certain percentage of photons at each spatial location, depending on the absorption rate ($\delta = 0.01$) and the probability density (intensity) of the ground-truth image (**Fig. 2b**).

To simulate excitation and emission PSFs as well as light-sheet thickness, we measured effective PSFs from fluorescent beads of a real multiview data set taken with the Zeiss SPIM prototype and a 40×/0.8-NA water-dipping objective. The attenuated image is subsequently convolved with a different PSF for each view (**Fig. 2b**).

To simulate the reduced axial resolution, we sampled every third slice in the axial (*z*) direction and every pixel in lateral direction (*xy*). This corresponds to the anisotropy of a typical multiview acquisition (**Supplementary Table 1**). The sampling process for each pixel is an individual Poisson process, with the intensity of the convolved pixel being its average (**Fig. 2b**).

To align all simulated views, we first scaled them to an isotropic volume and then rotated them back into the original orientation of the ground-truth data (**Fig. 2c**). Linear interpolation was used for all transformations.

**Nuclei-based registration of *C. elegans*.** In order to achieve a good deconvolution result, the individual views must be registered with very high precision. To achieve that, we match fluorescent beads that are embedded into the agarose with subpixel accuracy[14]. However, in *C. elegans* during larval stages, the cuticle itself acts as a lens, refracting the light sheet, which results in a slight misalignment of data inside the specimen. We therefore apply a secondary alignment step, which identifies corresponding nuclei in between views using redundant geometric local descriptor matching, and from that estimate an affine transformation model for each view correcting for the refraction due to the cuticle. The algorithm works similarly to the bead-based registration[14] and is implemented in Fiji[19] as a plug-in called "descriptor-based series registration" (S.P., unpublished software).

**Implementation details.** The simulation of multiview data (**Fig. 2**) and the 3D rendering (**Fig. 2a**) are implemented in ImgLib2 (ref. 20). The source code for the simulation is available as **Supplementary Software 1**; links to the current source code hosted on GitHub are available in the "readme" file and in **Supplementary Note 8**.

The multiview deconvolution is implemented in Fiji[19] using ImgLib2 (ref. 20). Performance-critical tasks are the convolutions with the PSFs or the compound kernels. They are implemented using Fourier convolutions, and an alternative implementation of Fourier convolution is provided for the GPU. Note that it is currently not possible to implement the entire pipeline on the GPU owing to the limited size of graphics card memory. All significant parts of the implementation including per-pixel operations, copy and paste of blocks and the fast Fourier transform are completely multithreaded to allow maximal execution performance on the CPU and GPU. The source code is available as **Supplementary Software 2**; links to the GitHub repository containing the current source code versions are listed in the "readme" file and in **Supplementary Note 8**. Please note that an updated version of the multiview deconvolution is already shipped within Fiji. To simply use the deconvolution, building the source code is not required; an updated Fiji[19] is sufficient.

The GPU implementation based on CUDA alternatively executes the Fourier convolution on Nvidia hardware. The native code is called via Java Native Access. The source code and precompiled libraries for CUDA5.5 for Windows 64 bit and CUDA5.0 for Linux 64 bit are available as **Supplementary Software 3**. Note that for Windows the DLL has to be placed in the Fiji directory; for Linux, in a subdirectory called lib/linux64; and that the current version of the Nvidia CUDA driver needs to be installed on the system.

The native CUDA code is platform dependent. If the provided precompiled libraries do not work, make sure you have the current Nvidia CUDA driver (https://developer.nvidia.com/cuda-downloads) installed and the Nvidia samples are working. If Fiji[19] still does not recognize the Nvidia CUDA capable devices,




doi:10.1038/nmeth.2929

compile the CUDA code from source. You can use CMAKE, which is set up to compile the code platform independently. Alternatively, it can be compiled using the following command under Linux: nvcc convolution3Dfft.cu --compiler-options '-fPIC' -shared -lcudart -lcufft -I/opt/cuda5/include/ -L/opt/cuda5/lib64 -lcuda -o libConvolution3D fftCUDAlib.so

**FIJI plug-ins.** The multiview deconvolution is integrated into Fiji[19] (http://fiji.sc/). Please make sure to update Fiji[19] before running the multiview deconvolution. The typical workflow consists of three steps.

1. Run the bead-based registration on the data (http://fiji.sc/SPIM_Bead_Registration).

2. Perform a simple average multiview fusion in order to define the correct bounding box on which the deconvolution should be performed (http://fiji.sc/Multi-View_Fusion).

3. Run the multiview deconvolution using either the GPU or the CPU implementation (http://fiji.sc/Multi-View_Deconvolution).

Detailed instructions for the individual plug-ins can be found on their respective Fiji wiki pages, summarized on this page http://fiji.sc/SPIM_Registration. Note that owing to the scripting capabilities of Fiji, the workflow can be automated and executed on a cluster (http://fiji.sc/SPIM_Registration_on_cluster). An example data set is available for download: http://fiji.sc/SPIM_Registration#Downloading_example_dataset.

21. Uddin, M.S., Lee, H.K., Preibisch, S. & Tomancak, P. *Microsc. Microanal.* **17**, 607–613 (2011).